Nano Research 2018, 11(7): 3854–3863
https://doi.org/10.1007/s12274-017-1959-7
Research Article
ISSN 1998-0124
CN 11-5974/O4

Bifunctional plasmonic colloidosome/graphene oxide-based floating membranes for recyclable high-efficiency solar-driven clean water generation

Minmin Wang[1,2], Jie Zhang[1], Ping Wang[1], Chuanping Li[1,2], Xiaolong Xu[1], and Yongdong Jin[1] (✉)

[1] *State Key Laboratory of Electroanalytical Chemistry, Changchun Institute of Applied Chemistry, Chinese Academy of Sciences, Changchun 130022, China*
[2] *University of Chinese Academy of Sciences, Beijing 100049, China*

Received: 27 September 2017
Revised: 6 December 2017
Accepted: 10 December 2017

KEYWORDS
plasmonic,
photothermal,
recyclable,
steam generation,
dye degradation

ABSTRACT

Utilizing plasmonic nano-particles/structures for solar water evaporation has aroused increasing interest; however, large-scale methods are desired to boost the efficiency and improve the practicality of solar steam generation. We developed a membrane-supported floating solar steam generation system based on graphene oxide and a multiscale plasmonic nanostructure; the latter is a micrometer-sized colloidosome that was assembled from hollow and porous Ag/Au nanocubes. By taking advantage of multiscale plasmonic coupling of the particles, an extremely high solar thermal conversion efficiency up to 92% at 10 $kW \cdot m^{-2}$ (with a water evaporation rate reaching 12.96 $kg \cdot m^{-2} \cdot h^{-1}$) can be achieved. The TiO_2 nanoparticle-modified floating system is also capable of high-efficiency dye degradation in organic-polluted water, rendering such a membrane system recyclable and scalable for practical and versatile solar-driven generation of clean water.

1 Introduction

Solar energy is an inexhaustible source of energy to alleviate the global energy and environmental crises [1, 2]. Utilizing solar energy for water evaporation was recently reconsidered as a highly efficient method to produce clean water and treat wastewater [3–7]. Efficient harvesting of solar energy is a key factor to design and select materials for this purpose; recently, efforts have been devoted to facilitate efficient steam generation under solar irradiation [3, 6, 8–12], e.g., by exploiting interfacial water heating instead of traditional low-efficiency bulk water heating [13, 14] and designing broadband solar receivers [3, 11, 15]. Graphene oxide (GO) is a promising candidate for its outstanding light absorption and excellent photothermal transduction; it has been used as a light absorber in solar-driven water evaporation processes [5, 12, 16, 17]. Plasmonic

Address correspondence to ydjin@ciac.ac.cn

nanoparticles (NPs), which show localized and tunable optical and photothermal properties [18–24], are another class of ideal nanomaterials for solar water heating [4, 25]. Although these studies have achieved relatively high evaporation efficiencies, better solar steam generation materials and design strategies are desired, and there is plenty of room for improvement toward practical applications.

Although plasmonic NPs with an efficient broadband solar absorption and photothermal conversion efficiency are crucial and highly desired for solar steam generation applications, classic plasmonic Au NPs or Ag NPs usually only display a narrow absorption bandwidth, which limits the broadband solar absorption [26]. Much effort has focused on finding plasmonic NPs with tunable and broad absorption [27, 28]. In this study, we designed and prepared Ag/Au nanocube (NC)-based plasmonic colloidosomes (Ag/Au PCs) as multiscale plasmonic nanostructures for solar steam generation to attain efficient solar light absorption and photothermal conversion. Although PCs have recently been successful for photothermal biomedical applications [29–31], no attempts have been reported for solar steam generation applications. Three-dimensional (3D) PCs are ideal plasmonic components for designing materials for solar steam generation because of their intense broadband light absorption from strong interparticle plasmonic coupling. To further enhance the light absorption and solar thermal conversion efficiency, we combined the use of Ag/Au PCs with a GO membrane as a light absorbing layer for solar steam generation. Meanwhile, to minimize the heat loss (to the bulk solution) and localize heating at the evaporating surface, the absorbent layer was physically separated by a floating polystyrene (PS) foam (thermal conductivity of ~ 0.04 W mK^{-1}).

Another promising and widely studied route to use solar energy for the purification of water is decontamination through photocatalytic processes. Solar-driven interfacial evaporation would significantly enhance the adsorption removal performance with the assistance of an upward vapor flow. Therefore, the high solar steam generation efficiency is beneficial for dye degradation in organic-polluted water.

In this study, we develop a membrane-supported floating solar steam generation system based on GO and a novel multiscale plasmonic nanostructure; the latter is a microscale PC that was assembled from Ag/Au hollow and porous nanocube (Ag/Au HPNC) monomers. By taking advantage of the multiscale plasmonic coupling of the PCs, an extremely high solar thermal conversion efficiency (up to 92% at 10 kW·m^{-2}) can be achieved. In addition to the excellent steam generation capability, the modified system also provides highly efficient dye degradation in organic-polluted water, rendering such a bifunctional membrane-supported solar steam generation system recyclable and scalable for practical and versatile solar-driven generation of clean water.

2 Experimental

2.1 Materials and chemicals

$AgNO_3$ and $NH_2OH·HCl$ were purchased from Sigma-Aldrich. $HAuCl_4·3H_2O$ was obtained from Beijing Chemical Works. Poly(diallyl dimethylammonium) chloride (PDDA) (20 wt.% in water, M_W = 100,000–200,000), $NH_3·H_2O$ (25%), and titanium oxide (P25) were purchased from Sinopharm Chemical Reagent Co., Ltd. All chemicals were used as received and without any further purification.

2.2 Synthesis of Ag nanocubes

Ag NCs were prepared by a hydrothermal method with slight modification [32]. In a typical experiment, 20 mL of $AgNO_3$ (20 mM), 1.1 mL of $NH_3·H_2O$ (25%), and 1.1 mL of PDDA (10 wt.%) were vigorously stirred for 0.5 h; then, the mixtures were transferred to 40-mL Teflon-sealed autoclaves and heated at 170 °C for 16 h. After the reaction, the autoclaves were cooled in air, and the suspensions were centrifuged for 20 min at 5,000 rpm; the precipitates were washed with purified water and centrifuged three times.

2.3 Synthesis of Ag/Au hollow and porous nanocubes

Ag/Au NCs were synthesized according to our previous method [33]. The prepared Ag sol (20 mL) was diluted with 20 mL of water; a freshly prepared reaction solution of 0.1% $HAuCl_4$ (500 μL) and 20 mM

NH_2OH (100 μL) was added to a glass vial with magnetic stirring. The solution was then heated and refluxed for 7–8 min before cooling to room temperature. Then, an excess of H_2O_2 (0.1 mol·L^{-1}) was added to the solution of Ag/Au hollow NCs, and the reaction proceeded at room temperature for several minutes.

2.4 Synthesis of Ag/Au plasmonic colloidosomes

The colloidosomes were synthesized by a self-assembly process as previous reported with slight modification [34]. In a typical preparation process, the concentration of the as-prepared Ag/Au HPNCs was concentrated to 2 mM. Then, 10 mL of 1-butanol was added to the colloidal suspension (ratio of 1-butanol to water of 10:1). Then, the mixture was emulsified by shaking and ultrasonication. These Au/Ag NPs spontaneously absorbed at the emulsion interface; this was driven by minimizing the total interfacial free energy [35]. Finally, the self-assembled colloidosomes were obtained by naturally settling on the bottom of the container.

2.5 Preparation of graphene oxide

GO was prepared using the improved Hummers method [36] with a slight modification. Typically, a 9:1 mixture of concentrated H_2SO_4/H_3PO_4 (360:40 mL) was added to a mixture of graphite flakes (3.0 g) and $KMnO_4$ (18.0 g). The reaction was then heated to 65 °C and stirred for 12 h. Then, the reaction was cooled to room temperature; 400 mL of ice with 30% H_2O_2 (3 mL) was poured onto the solution, and the mixture was washed with 5% HCl. Finally, the mixture was washed with deionized water until the pH of the solution was neutral.

2.6 Fabrication processes for the steam generation devices

The GO solution (5 mL; 4 mg·mL^{-1}) was deposited onto a porous mixed cellulose membrane filter (50 mm in diameter, 0.45-μm pore size) to form a GO film through vacuum filtration; the PC/GO and P25/PC/GO films were prepared similarly by adding 5 mL of additional Ag/Au PCs (2 μM) and P25 + Ag/Au PC (2 μM) colloidal solutions, respectively, to the GO films during the mild vacuum filtration process. Then, the films were naturally dried at room temperature. A PS foam (~ 2-cm thick) was chosen as the supporting material for preparing the floating devices. Meanwhile, the PS foam was wrapped with a clean fiber cloth to ensure that the water could reach the upper surface of the PS foam.

2.7 Equipment and characterization

Ultraviolet–visible (UV–Vis) absorption spectra were measured using a Cary 500 Scan UV-Vis spectrophotometer (Varian, USA). The detailed microstructure and chemical composition of the samples were investigated by field emission scanning electron microscopy (SEM) using a Hitachi S4800 microscope operated at 10 kV and transmission electron microscopy (TEM) using a JEOL 2010 microscope operated at an accelerating voltage of 200 kV and equipped with an energy dispersive spectrometer. X-ray photoelectron spectroscopy (XPS) was performed on an X-ray photoelectron spectrometer (ESCALAB 250 Xi, Thermo Fisher Scientific). Infrared spectra were measured on a VERTEX 70 Fourier transform infrared (FTIR) spectrometer (Bruker). An inductively coupled plasma (ICP) atomic emission spectrometer and mass spectrometer (iCAP 6000 Series, ICP spectrometer, Thermo Scientific) were used to determine the concentration of NPs. A 300-W xenon lamp equipped with a filter of $\lambda > 420$ nm (10 kW·m^{-2}) was used for the illumination experiments.

3 Results and discussion

As schematically illustrated in Fig. 1(b), the top membrane of the PC-loaded GO acts as a light absorber under illumination to efficiently harvest and convert light to thermal energy. In the material configuration, the Ag/Au PCs with broadband absorption form many internal hot spots where evaporation occurs, and the GO film can provide an efficient path for water supply and vapor flow in addition to absorbing light. The synergistic effect between the PCs and GO film greatly promote the capture and conversion of solar energy; the PS foam in the bottom acts as an excellent thermal barrier to minimize heat transfer to the non-evaporative bulk water.

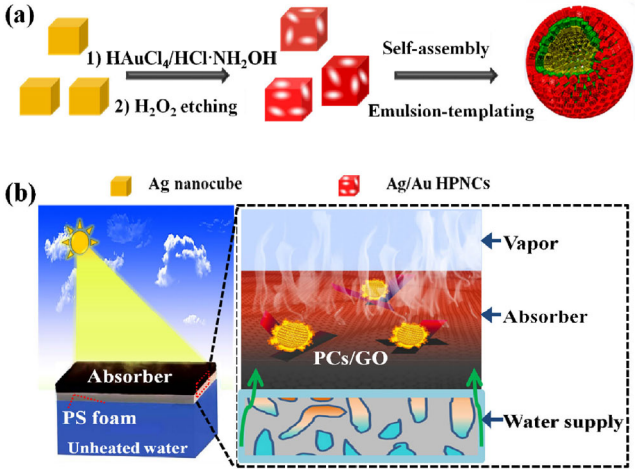

Figure 1 (a) Schematics of PC preparation. (b) Schematics of a floating PC/GO membrane-based device for solar steam generation: the PC/GO film serves as a light absorber and converts sunlight into vapor on the top; the floating PS foam supports the PC/GO film and suppresses heat loss to the non-evaporative bulk water.

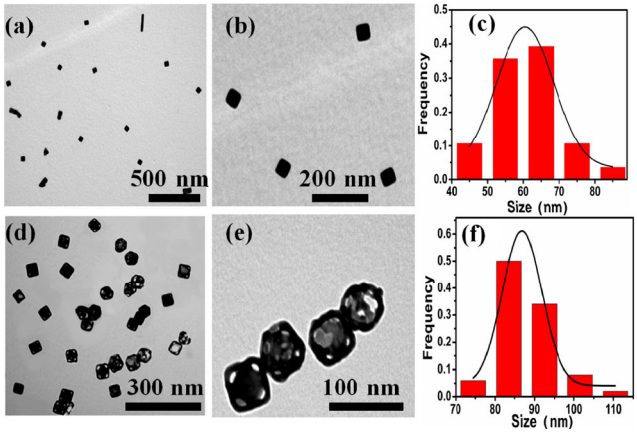

Figure 2 (a) and (b) TEM images of the precursor Ag NCs and (c) their corresponding particle size distribution. (d) and (e) TEM images of the Ag/Au HPNCs and (f) their corresponding particle size distribution.

The 3D micro-sized spherical PCs are composed of Ag/Au HPNCs. The Ag/Au HPNCs were first prepared from the pre-synthesized precursor Ag NCs [32] according to our previous method [33]. The detailed synthetic procedures are described in the Experimental section. The morphology of the as-prepared Ag NCs and Ag/Au HPNCs were characterized by TEM. As shown in Figs. 2(a) and 2(b), the as-prepared precursor Ag NCs are nearly monodispersed with sharp corners and an average edge length of ~ 60 nm (Fig. 2(c)); the as-prepared Ag/Au HPNCs show hollow and porous characteristics (Figs. 2(d) and 2(e)) with a mean diameter of ~ 87 nm (Fig. 2(f)). The XPS spectrum of the as-prepared Ag/Au HPNCs was analyzed. As shown in Fig. S1 in the Electronic Supplementary Material (ESM), two characteristic peaks arising from the Ag $3d_{5/2}$ and Ag $3d_{3/2}$ orbitals are located at 368.3 and 374.3 eV, respectively; meanwhile, the orbitals of Au $4f_{7/2}$ and Au $4f_{5/2}$ are located at 82.3 and 85.9 eV, respectively, suggesting that Ag and Au in the as-prepared Ag/Au HPNCs are present in the metallic state. The Ag/Au molar ratio of the as-prepared Ag/Au HPNCs was estimated to be ~ 2.5 (Fig. S1(c) in the ESM).

Spherical micro-sized Ag/Au PCs were prepared by self-assembly from the as-prepared Ag/Au HPNCs via an emulsion-templating strategy [34]. Figures 3(a)–3(d) show typical SEM images of the resultant Ag/Au PCs. The obtained PCs have a size distribution ranging from ~ 1 to 5 μm (Figs. 3(a) and 3(b)) with a mean diameter of 3 μm (Fig. S2 in the ESM). Most show an intact spherical shape, and only a few have chipped edges. The images of the collapsed PCs (Figs. 3(c) and 3(d)) show that the resultant PCs are composed of a multilayered NP shell and a hollow cavity, of which the hollow and porous characteristic of the unit Ag/Au HPNCs are visible. The hollow and porous structure of the unit Ag/Au HPNCs was observable from the rim of a single colloidosome by TEM analysis, as shown in Fig. S3 in the ESM. Moreover, the Ag/Au bimetallic nature of the PCs was further confirmed by SEM elemental mapping analysis. As shown in Fig. S4 in the ESM, Ag and Au were homogeneously distributed throughout the as-prepared PCs. Figure 3(e) shows the absorption spectra of the obtained Ag NCs, Ag/Au HPNCs, and Ag/Au PCs, respectively. The Ag NCs have one localized surface plasmon resonance (LSPR) peak centered at ~ 466 nm, while the absorption peak of the Ag/Au HPNCs appeared at a longer wavelength, shifted toward 713 nm. After assembly into micro-sized PCs, the LSPR peak centered at 466 or 713 nm diminished, but a significantly enhanced broad plasmon absorption band appeared in the visible to near-infrared (NIR) region because of the strong plasmonic coupling among the Ag/Au HPNCs in the PC shell.

To assess the photothermal conversion efficiency

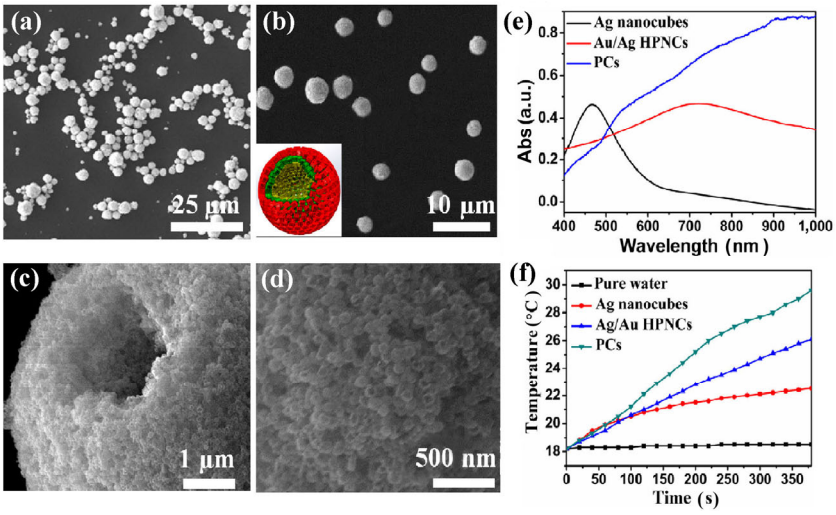

Figure 3 (a)–(d) SEM images of the as-prepared Ag/Au PCs. (e) Absorption spectra of Ag NCs, Ag/Au HPNCs, and Ag/Au PCs, respectively. (f) NIR-induced heat generation of pure H_2O, and Ag NCs, Ag/Au HPNCs, and Ag/Au PCs containing an aqueous solution at laser power densities of 1.2 W·cm^{-2} with the same unit NP concentration (~ 5.5 × 10^{10} particles·mL^{-1}).

of the particles, a laser irradiation experiment was conducted at a wavelength of 808 nm; this wavelength corresponds with the LSPR of the PCs. For comparison, the particle solutions containing Ag/Au PCs or their precursor Ag/Au NPs with the same concentration of unit NPs (~ 5.5 × 10^{10} particles·mL^{-1}, 5 mL) were used for this experiment and performed at the same laser power densities of 1.2 W·cm^{-2}. As shown in Fig. 3(f), the temperature of all three particle solutions increased rapidly upon laser irradiation and then decreased gradually to reach thermal equilibrium. The Ag/Au PC solution displays the highest photothermal conversion ability for bulk solution heating because of intense broadband absorption caused by the strong interparticle plasmonic coupling; the temperature is ~ 40% higher than that observed for the precursor Ag/Au HPNCs. Meanwhile, for comparison, we also conducted a photothermal conversion efficiency test using 650- and 450-nm laser irradiation. As shown in Fig. S5 in the ESM, though there is some decrease in ΔT (T = temperature) caused by off-resonance irradiation of the sample, the PCs also showed a good photothermal conversion efficiency because of their intense broadband absorption property caused by the strong interparticle plasmonic coupling. Therefore, the as-prepared Ag/Au PCs were used for subsequent solar steam generation.

To further enhance the solar thermal conversion efficiency and facilitate their potential for practical use, we tried complexing the Ag/Au PCs with GO films, which are efficient and broadband light absorbers that were fabricated by a low-cost and scalable process [37]; meanwhile, the rich functional groups of GO facilitate the combination with Ag/Au PCs. The existence of oxygen-containing groups on the surface of GO was examined by FTIR. As shown in Fig. 4(a), the strong and broad peak around 3,422 cm^{-1} in the FTIR spectrum is attributed to –OH, while the sharp peaks at 1,744 and 1,628 cm^{-1} originate from C=O and C–C, respectively. The characteristic peak at 1,223 cm^{-1} is due to vibration of the C–OH group [38]. Figure 4(b) shows the XPS spectrum of the GO film. The 1s peak of carbon (C1s) of the GO film mainly consists of four types of carbon bonds [37, 39]: C–C (aromatic rings) at ~ 283.6 eV, C–O (hydroxyl and epoxy) at ~ 286.1 eV, C=O (carbonyl) at ~ 288.1 eV, and O–C=O (carboxyl) at ~ 289.7 eV. Figure 4(c) shows an optical picture of the as-prepared PC/GO film. In a typical procedure, 5 mL of a 4 mg·mL^{-1} oxidized graphene solution was mixed with Ag/Au PCs and gently vacuum dried (to avoid severe aggregation and damage of the Ag/Au PCs) in a vacuum suction apparatus using a mixed fiber membrane with a 0.45-μm pore size as a flexible substrate. Then we transferred the dried PC/GO membrane (with a diameter of 36 mm) onto a PS foam, which was

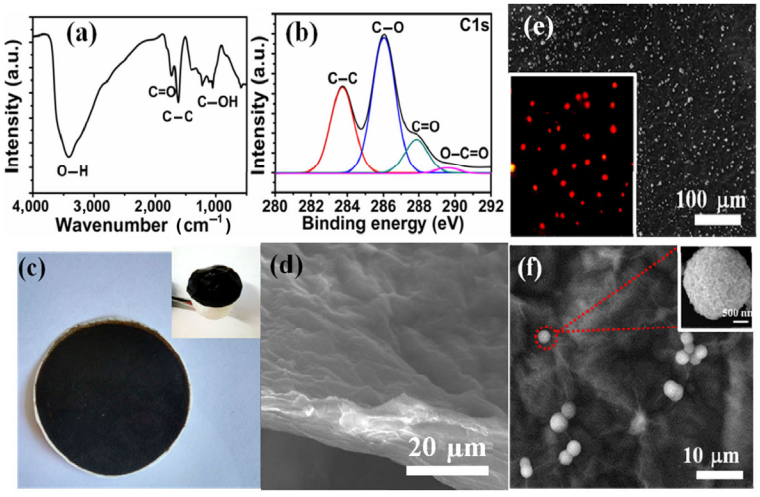

Figure 4 (a) FTIR spectrum of GO. (b) XPS spectra and curve fitting of the C1s spectra of GO. (c) Optical image of the black PC/GO film on a white PS foam with a diameter of 36 mm. (d) SEM image of the GO film. (e) and (f) SEM images of the outermost surface of a PC/GO film and dark-field LSPR scattering images of the PCs ((e), inset).

wrapped over a layer of clean fiber cloth to provide a two-dimensional water path, as shown by the image in Fig. 4(c) (and the inset). As mentioned above, the PS foam serves as an effective heat barrier between the absorber and bulk water. Figures 4(d) and 4(e) show representative SEM images of vacuum-filtered multilayered GO thin films with a typical thickness of ~ 4 μm, without or after loading with Ag/Au PCs, respectively. The inset in Fig. 4(e) shows a typical plasmonic dark-field scattering images of the plasmonic PCs. As shown in Fig. 4(f), the Ag/Au PCs are still intact (see the inset in Fig. 4(f)) and well-deposited on the surface of the multilayered GO films.

We then systematically evaluated the solar-driven steam generation efficiency of our system by measuring the rate of water evaporation of the PC/GO/PS floating device by recording the water weight loss over time under solar illumination (10 kW·m^{-2}). Figure S6 in the ESM shows an optical image of our steam-generating device. The transmittance spectra of the GO and PC/GO films were carefully measured from 200 to 2,500 nm using UV–Vis spectroscopy. As shown in Fig. S7 in the ESM, the GO and PC/GO films both show a low transmittance. The PC/GO film has a lower transmittance in the NIR region, which was induced by the NIR plasmon absorption of the PCs. Figure 5(a) shows that the weight loss by water evaporation increases as a function of the irradiation time; the

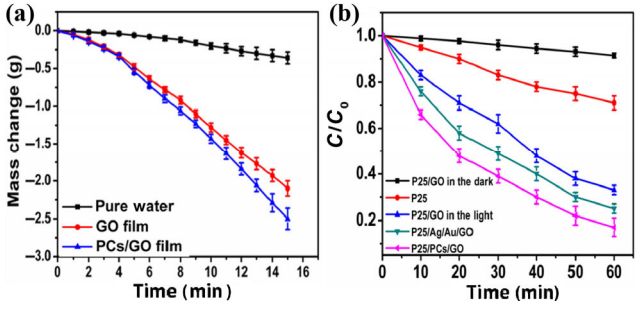

Figure 5 (a) Mass changes over time through steam generation under solar irradiation (10 kW·m^{-2}). (b) Photocatalytic curves of MB dye by P25, P25/GO, P25/Ag/Au/GO, and P25/PC/GO under visible light ($\lambda > 420$ nm), and the adsorption curve of P25/GO in the dark.

water evaporation rates of our device and pure GO film (PCs-free) are 12.96 and 9.98 kg·m^{-2}·h^{-1}, respectively, which are significantly higher than that for the pure water system (without the assistance of PCs or GO) under the same solar irradiation condition (~ 1.08 kg·m^{-2}·h^{-1}). The formula $\eta = \dot{m}h_{LV}/I$ was used to calculate the efficiency (η) [40], in which $\dot{m}$ is the mass flux, h_{LV} denotes the total enthalpy of the sensible heat and liquid–vapor phase change, and I is the power density of light irradiation [5, 10]. The energy transfer efficiency for the PC/GO film can reach 92%, which is higher than that for the pure floating GO films (71%). The improvement in the performance of the PC/GO film is attributed to the hollow and porous nanostructured nature of the unit

Ag/Au HPNCs and their strong interparticle plasmonic coupling in the colloidosomes, which induces an enhanced broadband light trapping/harvesting and hence photothermal conversion efficiency. Besides the high-efficiency photothermal conversion, the complex and multilevel hollow structures of the PCs and membrane facilitate upward vapor flow and benefit interfacial steam generation. Figure S8 in the ESM shows thermal images of the GO and PC/GO films at the same illumination time (recorded using an infrared camera). At the same illumination time, the PC/GO film generates more heat.

TiO_2 has been extensively used in photocatalysis for its superior chemical stability and nontoxicity. As shown in Fig. S9 in the ESM, the TiO_2 powder (P25 Degussa) has a particle size of ~ 25 nm, and the TiO_2 NPs (P25) absorb in the wavelength range of 200–350 nm. Consequently, only the UV fraction of the solar irradiation (about 5%) is active in the photoexcitation processes using pure P25. Herein, we deposited TiO_2 NPs (P25) on the surface of the as-prepared PC/GO films to investigate the photocatalytic performance of our plasmonic steam generation system for possible solar-driven cleaning of organic-polluted water. Figure S10(a) in the ESM shows the X-ray diffraction patterns of pure P25 and P25/PC/GO. The diffraction peaks for GO and the NPs are clearly seen in the patterns. Meanwhile, the UV absorption also indicates the existence of NPs and GO (Fig. S10(b) in the ESM) [41, 42]. In the experiments, a bifunctional membrane consisting of TiO_2 NPs (P25), PCs, and GO was prepared by simply dropping the P25 aqueous solution (1 mg·mL^{-1}) onto the surface of the preformed PC/GO films during membrane preparation by vacuum filtration and used for photocatalytic degradation of methylene blue (MB, C_0 = 10 mg·L^{-1}). In the typical photocatalytic experiment, the composite P25/PC/GO, P25/GO, P25/Ag/Au/GO, and pure P25 films were each immersed in a 20-mL MB solution. For each experiment, 5 mg of the photocatalyst (P25) was used. The reaction constant, k, was used to evaluate the degradation rate [43]. As shown in Fig. 5(b), the degradation rate is substantially higher for P25/GO (k = 1.89 × 10^{-2} min^{-1}) than for pure P25 (k = 0.57 × 10^{-2} min^{-1}). The composite film of P25/GO with pure Ag/Au NPs (k = 2.28 × 10^{-2} min^{-1}) showed a higher degradation rate than the pure P25/GO film, but an inferior degradation rate than P25/PC/GO (k = 2.71 × 10^{-2} min^{-1}). The GO in the composite P25/PC/GO film can help to remove contaminants through adsorption. Meanwhile, the high steam generation efficiency accelerates the upward diffusion of contaminants toward the floating composites and thus significantly speeds the removal of pollutants. The PCs with broadband absorption facilitate the photodegradation activity in visible light (Fig. S11 in the ESM).

As shown in Fig. 6(a), the plot of ln(C_0/C) against the irradiation time (t) is nearly linear, indicating a first-order reaction for the photocatalytic process. The photocatalytic ability of the P25/PC/GO membrane is also significantly enhanced for the degradation of MB by introducing Ag/Au PCs, of which the plasmonic photothermal effect facilitates the solar-driven interfacial evaporation process and accelerates the upward diffusion of contaminants toward the floating membrane composites. In contrast, light-induced intense local electric fields near the surface of the PCs benefit electron–hole pair generation in P25 and enhance the photocatalytic process [44–46].

As seen from the adsorption curve of P25/GO in the dark (Fig. 5(b)), P25/GO displays an excellent adsorption capacity because of the good adsorption properties of the GO films, which adsorbed ~ 10% of MB within 60 min without light irradiation. Nevertheless, this adsorption capacity is much lower than the photodegradation quantity under same time duration, indicating that the photocatalytic activity is the main driving force in the process. More importantly, the floatable photocatalyst materials and

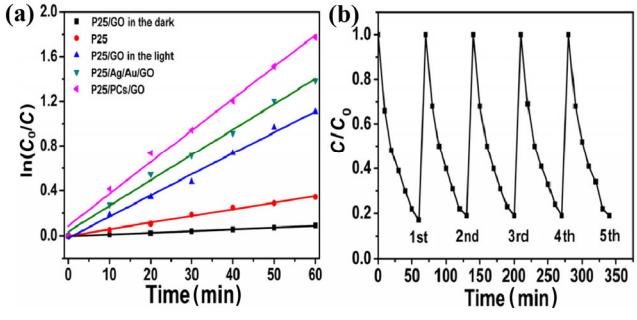

Figure 6 (a) First-order plots for the photodegradation of MB over P25, P25/GO, P25/Ag/Au/GO, and P25/PC/GO. (b) Five successive photodegradation dynamic curves of MB over P25/PC/GO.

device in our system can be reused by simply rinsing and transferring them into another photocatalytic cycle; this avoids time-consuming sample separation and treatment processes that are usually needed for solution-dispersed metallic NPs as the working medium. As shown in Fig. 6(b), the photocatalytic performance of the as-prepared floating P25/PC/GO membrane/device basically remains unchanged after five successive photocatalytic cycles. To clarify the elemental and chemical state of Ag in the sample after 5 h of continuous illumination, XPS spectra were collected. As shown in Fig. S12 in the ESM, the splitting of the 3d doublet occurs at 6.1 eV after 5 h of continuous illumination, indicating that the Ag particles inside both the pure PCs and P25/PCs maintain their metallic nature [47]. After continuous illumination, the $3d_{5/2}$ peak of Ag shifted to a lower binding energy. The binding energy shift of Ag can be mainly attributed to its alloying with Au and further electron transfer from the metal to TiO_2, forming monovalent Ag [48]. This indicates that the metal particles are in contact with the TiO_2 particles in our system, which facilitate electron transfer and effectively improve the photocatalytic degradation efficiency.

4 Conclusions

In conclusion, we developed a highly efficient photothermal membrane with broadband solar absorption by combining two excellent solar harvesting materials: plasmonic Ag/Au HPNC-based colloidosomes and GO films. A high-efficiency steam generation with a solar thermal conversion efficiency up to 92% at 10 $kW \cdot m^{-2}$ was realized by placing the GO/PC photothermal membrane on the top surface of the floating PS foam to form an effective device for practical use. The PS foam in the bottom acts as an excellent thermal barrier to minimize heat transfer to the non-evaporative bulk water. We propose that the multiscale plasmonic couplings of the microscale PCs that are composed of nanoscale Ag/Au HPNCs strongly contribute to enhance the efficiency. Furthermore, when incorporating TiO_2 NPs into the GO/PCs membrane, the resulting bifunctional membrane and floating device showed also excellent photocatalytic ability that was capable of highly efficient dye degradation for organic-polluted water. The rationally designed membrane-supported bifunctional plasmonic solar steam generation system and floating device are very promising for practical and versatile solar-driven clean water generation because of the excellent stability and reproducibility, and facile operation.

Acknowledgements

This work was financially supported by the National Natural Science Foundation of China (Nos. 21475125 and 21175125), the Hundred Talents Program of the Chinese Academy of Sciences, and the State Key Laboratory of Electroanalytical Chemistry (No. 110000R387).

Electronic Supplementary Material: Supplementary material (further details of the characterization of samples before and after sensing) is available in the online version of this article at https://doi.org/10.1007/s12274-017-1959-7.

References

[1] Bahnemann, D. Photocatalytic water treatment: Solar energy applications. *Solar Energy* **2004**, *77*, 445–449.

[2] Green, M. A.; Bremne, S. P. Energy conversion approaches and materials for high-efficiency photovoltaics. *Nat. Mater.* **2016**, *16*, 23–34.

[3] Zhou, L.; Tan, Y. L.; Wang, J. Y.; Xu, W. C.; Yuan, Y.; Cai, W. S.; Zhu, S. N.; Zhu, J. 3D self-assembly of aluminium nanoparticles for plasmon-enhanced solar desalination. *Nat. Photonics* **2016**, *10*, 393–398.

[4] Zheng, X. Z.; Zhang, L. W. Photonic nanostructures for solar energy conversion. *Energ. Envir. Sci.* **2016**, *9*, 2511–2532.

[5] Ghasemi, H.; Ni, G.; Marconnet, A. M.; Loomis, J.; Yerci, S.; Miljkovic, N.; Chen, G. Solar steam generation by heat localization. *Nat. Commun.* **2014**, *5*, 4449.

[6] Ni, G.; Li, G.; Boriskina, S. V.; Li, H. X.; Yang, W. L.; Zhang, T. J.; Chen, G. Steam generation under one sun enabled by a floating structure with thermal concentration. *Nat. Energy* **2016**, *1*, 16126.

[7] Elimelech, M.; Phillip, W. A. The future of seawater desalination: Energy, technology, and the environment. *Science* **2011**, *333*, 712–717.

[8] Liu, Y. M.; Yu, S. T.; Feng, R.; Bernard, A.; Liu, Y.; Zhang, Y.; Duan, H. Z.; Shang, W.; Tao, P.; Song, C. Y.; Deng, T. A bioinspired, reusable, paper-based system for high-performance large-scale evaporation. *Adv. Mater.* **2015**, *27*, 2768–2774.

[9] Zhou, L.; Tan, Y. L.; Ji, D. X.; Zhu, B.; Zhang, P.; Xu, J.; Gan, Q. Q.; Yu, Z. F.; Zhu, J. Self-assembly of highly efficient, broadband plasmonic absorbers for solar steam generation. *Sci. Adv.* **2016**, *2*, 1501227.

[10] Wang, Z. H.; Liu, Y. M.; Tao, P.; Shen, Q. C.; Yi, N.; Zhang, F. Y.; Liu, Q. L.; Song, C. Y.; Zhang, D.; Shang, W. et al. Bio-inspired evaporation through plasmonic film of nanoparticles at the air-water interface. *Small* **2014**, *10*, 3234–3239.

[11] Bae, K.; Kang, G. M.; Cho, S. K.; Park, W.; Kim, K.; Padilla, W. J. Flexible thin-film black gold membranes with ultrabroadband plasmonic nanofocusing for efficient solar vapour generation. *Nat. Commun.* **2015**, *6*, 10103.

[12] Ito, Y.; Tanabe, Y.; Han, J. H.; Fujita, T.; Tanigaki, K.; Chen, M. W. Multifunctional porous graphene for high-efficiency steam generation by heat localization. *Adv. Mater.* **2015**, *27*, 4302–4307.

[13] Zhang, L. B.; Tang, B.; Wu, J. B.; Li, R. Y.; Wang, P. Hydrophobic light-to-heat conversion membranes with self-healing ability for interfacial solar heating. *Adv. Mater.* **2015**, *27*, 4889–4894.

[14] Yu, S. T.; Zhang, Y.; Duan, H. Z.; Liu,Y. M.; Quan, X. J.; Tao, P.; Shang, W.; Wu, J. B.; Song, C. Y.; Deng, T. The impact of surface chemistry on the performance of localized solar-driven evaporation system. *Sci. Rep.* **2015**, *5*, 13600.

[15] Ni, G.; Miljkovic, N.; Ghasemi, H.; Huang, X. P.; Boriskina, S. V.; Lin, C. T.; Wang, J. J.; Xu, Y. F.; Rahman, M. M.; Zhang, T. J. et al. Volumetric solar heating of nanofluids for direct vapor generation. *Nano Energy* **2015**, *17*, 290–301.

[16] Shi, L.; Wang, Y. C.; Zhang, L. B.; Wang, P. Rational design of a bi-layered reduced graphene oxide film on polystyrene foam for solar-driven interfacial water evaporation. *J. Mater. Chem. A* **2017**, *5*, 16212–16219.

[17] Surwade, S. P.; Smirnov, S. N.; Vlassiouk, I. V.; Unocic, R. R.; Veith, G. M.; Dai, S.; Mahurin, S. M. Water desalination using nanoporous single-layer graphene. *Nat. Nanotechnol.* **2015**, *10*, 459–464.

[18] Jin, Y. D.; Jia, C. X.; Huang, S. W.; O'Donnell, M.; Gao, X. H. Multifunctional nanoparticles as coupled contrast agents. *Nat. Commun.* **2010**, *1*, 41.

[19] Jin, Y. D.; Gao, X. H. Plasmonic fluorescent quantum dots. *Nat. Nanotechnol.* **2009**, *4*, 571–576.

[20] Jin, Y. D. Multifunctional compact hybrid Au nanoshells: A new generation of nanoplasmonic probes for biosensing, imaging, and controlled release. *Acc. Chem. Res.* **2014**, *47*, 138–148.

[21] Shi, L.; Zhu, L. Y.; Guo, J.; Zhang, L. J.; Shi, Y. N.; Zhang, Y.; Hou, K.; Zheng, Y. L.; Zhu, Y. F.; Lv, J. W. et al. Self-assembly of chiral gold clusters into crystalline nanocubes of exceptional optical activity. *Angew. Chem., Int. Ed.* **2017**, *27*, 15397–15401.

[22] Han, B.; Shi, L.; Gao, X. Q.; Guo, J.; Hou, K.; Zheng, Y. L.; Tang, Z. Y. Ultra-stable silica-coated chiral Au-nanorod assemblies: Core–shell nanostructures with enhanced chiroptical properties. *Nano Res.* **2016**, *9*, 451–457.

[23] Wang, P. L.; Lin, Z. Y.; Su, X. O.; Tang, Z. Y. Application of Au based nanomaterials in analytical science. *Nanotoday* **2017**, *12*, 64–97.

[24] Liu, X.; He, L. C.; Zheng, J. Z.; Guo, J.; Bi, F.; Ma, X.; Zhao, K.; Liu, Y. L.; Song, R.; Tang, Z. Y. Solar-light-driven renewable butanol separation by core–shell Ag@ZIF-8 nanowires. *Adv. Mater.* **2015**, *27*, 3273–3277.

[25] Neumann, O.; Urban, A. S.; Day, J.; Lal, S.; Nordlander, P.; Halas, N. J. Solar vapor generation enabled by nanoparticles. *ACS Nano* **2013**, *7*, 42–49.

[26] Aydin, K.; Ferry, V. E.; Briggs, R. M.; Atwater, H. A. Broadband polarization-independent resonant light absorption using ultrathin plasmonic super absorbers. *Nat. Commun.* **2011**, *2*, 517.

[27] Xiong, W.; Sikdar, D.; Yap, L. W.; Premaratne, M.; Li, X. Y.; Cheng, W. L. Multilayered core-satellite nanoassemblies with fine-tunable broadband plasmon resonances. *Nanoscale* **2015**, *7*, 3445–3452.

[28] Xiong, W.; Sikdar, D.; Walsh, M.; Si, K. J.; Tang, Y.; Chen, Y.; Mazid, R.; Weyland, M.; Rukhlenko, I. D.; Etheridge, J. et al. Single-crystal caged gold nanorods with tunable broadband plasmon resonances. *Chem. Commun.* **2013**, *49*, 9630–9632.

[29] Lin, J.; Wang, S. J.; Huang, P.; Wang, Z.; Chen, S. H.; Niu, G.; Li, W. W.; He, J.; Cui, D. X.; Lu, G. M. et al. Photosensitizer-loaded gold vesicles with strong plasmonic coupling effect for imaging-guided photothermal/photodynamic therapy. *ACS Nano* **2013**, *7*, 5320–5329.

[30] Huang, P.; Lin, J.; Li, W. W.; Rong, P. F.; Wang, Z.; Wang, S. J.; Wang, X. P.; Sun, X. L.; Aronova, M.; Niu, G. et al. Biodegradable gold nanovesicles with an ultrastrong plasmonic coupling effect for photoacoustic imaging and photothermal therapy. *Angew. Chem., Int. Ed.* **2013**, *125*, 14208–14214.

[31] Song, J. B.; Cheng, L.; Liu, A. P.; Yin, J.; Kuang, M.; Duan, H. W. Plasmonic vesicles of amphiphilic gold nanocrystals: Self-assembly and external-stimuli-triggered destruction. *J. Am. Chem. Soc.* **2011**, *133*, 10760–10763.

[32] Chen, H. J.; Wang, Y. L.; Dong, S. J. An effective hydrothermal route for the synthesis of multiple PDDA-protected noble-metal nanostructures. *Inorg. Chem.* **2007**, *46*, 10587–10593.

[33] He, H. L.; Xu, X. L.; Wu, H. X.; Jin, Y. D. Enzymatic plasmonic engineering of Ag/Au bimetallic nanoshells and their use for sensitive optical glucose sensing. *Adv. Mater.* **2012**, *24*, 1736–1740.

[34] Liu, D. L.; Zhou, F.; Li, C. C.; Zhang, T.; Zhang, H. H.; Cai, W. P.; Li, Y. Black gold: Plasmonic colloidosomes with broadband absorption self-assembled from monodispersed gold nanospheres by using a reverse emulsion system. *Angew. Chem., Int. Ed.* **2015**, *54*, 9596–9600.

[35] Mao, Z. W.; Xu, H. L.; Wang, D. Y. Molecular mimetic self-assembly of colloidal particles. *Adv. Funct. Mater.* **2010**, *20*, 1053–1074.

[36] Marcano, D. C.; Kosynkin, D. V.; Berlin, J. M.; Sinitskii, A.; Sun, Z. Z.; Slesarev, A.; Alemany, L. B.; Lu, W.; Tour, J. M. Improved synthesis of graphene oxide. *ACS Nano* **2010**, *4*, 4806–4814.

[37] Li, X. Q.; Xu, W. C.; Tang, M. Y.; Zhou, L.; Zhu, B.; Zhu, S. N.; Zhu, J. Graphene oxide-based efficient and scalable solar desalination under one sun with a confined 2D water path. *Proc. Natl. Acad. Sci. USA* **2016**, *113*, 13953–13958.

[38] Ramasamy, M. S.; Mahapatra, S. S.; Yoo, H. J.; Kim, Y. A.; Cho, J. W. Soluble conducting polymer-functionalized graphene oxide for air-operable actuator fabrication. *J. Mater. Chem. A* **2014**, *2*, 4788–4794.

[39] Boukhvalov, D. W.; Katsnelson, M. I. Modeling of graphite oxide. *J. Am. Chem. Soc.* **2008**, *130*, 10697–10701.

[40] Jiang, Q. S.; Tian, L. M.; Liu, K. K.; Tadepalli, S.; Raliya, R.; Biswas, P.; Naik, R. R.; Singamaneni, S. Bilayered biofoam for highly efficient solar steam generation. *Adv. Mater.* **2016**, *28*, 9400–9407.

[41] Xu, Z. C.; Hou, Y. L.; Sun, S. H. Magnetic core/shell Fe_3O_4/Au and Fe_3O_4/Au/Ag nanoparticles with tunable plasmonic properties. *J. Am. Chem. Soc.* **2007**, *129*, 8698–8699.

[42] Zhang, J. L.; Yang, H. J.; Shen, G. X.; Cheng, P.; Zhang J. Y.; Guo, S. W. Reduction of graphene oxide via L-ascorbic acid. *Chem. Commun.* **2010**, *46*, 1112–1114.

[43] Fan, Y. Y.; Ma, W. G.; Han, D. X.; Gan, S. Y.; Dong, X. D.; Niu, L. Convenient recycling of 3D AgX/graphene aerogels (X = Br, Cl) for efficient photocatalytic degradation of water pollutants. *Adv. Mater.* **2015**, *27*, 3767–3773.

[44] Tatsuma, T.; Nishi, H.; Ishida, T. Plasmon-induced charge separation: Chemistry and wide applications. *Chem. Sci.* **2017**, *8*, 3325–3337.

[45] Du, J.; Qi, J.; Wang, D.; Tang, Z. Y. Facile synthesis of Au@TiO_2 core–shell hollow spheres for dye-sensitized solar cells with remarkably improved efficiency. *Energy Environ. Sci.* **2012**, *5*, 6914–6918.

[46] Brongersma, M. L.; Halas, N. J.; Nordlander, P. Plasmon-induced hot carrier science and technology. *Nat. Nanotechnol.* **2015**, *10*, 25–34.

[47] Lin, D. D.; Wu, H.; Zhang, R.; Pan, W. Enhanced photocatalysis of electrospun Ag-ZnO heterostructured nanofibers. *Chem. Mater.* **2009**, *21*, 3479–3484.

[48] Liu, H. R.; Shao, G. X.; Zhao, J. F.; Zhang, Z. X.; Zhang, Y.; Liang, J.; Liu, X. G.; Jia, H. S.; Xu, B. S. Worm-like Ag/ZnO core–shell heterostructural composites: Fabrication, characterization, and photocatalysis. *J. Phys. Chem. C* 2012, *116*, 16182–16190.